to be published in European Physical Journal E (2006)

External field-induced switching in nematic elastomers: a Monte Carlo study

G. Skačej[1,2] and C. Zannoni[1]

[1] Dipartimento di Chimica Fisica ed Inorganica and INSTM, Università di Bologna, Viale Risorgimento 4, I-40136 Bologna, Italy

[2] Oddelek za fiziko, Univerza v Ljubljani, Jadranska 19, SI-1000 Ljubljana, Slovenia

Received: date / Revised version: date

Abstract. We present a Monte Carlo study of external field-induced switching in nematic elastomers, employing a coarse-grained shearable lattice model. In large enough systems a full-wavelength Fréedericksz effect is observed — as opposed to the half-wavelength effect seen in ordinary nematics — that clearly reflects in simulated polarized light textures, as well as in deuterium magnetic resonance spectra. The reorientation of mesogenic units is accompanied by pronounced shear deformations.

PACS. 61.30.Vx Polymer liquid crystals – 61.30.Cz Molecular and microscopic models and theories of liquid crystal structure – 61.41.+e Polymers, elastomers, and plastics

1 Introduction

Nematic elastomers — crosslinked polymeric chains with embedded mesogenic units — are rubberlike materials where mechanical deformations and orientational ordering are strongly coupled [1]. As the orientation of mesogenic units can be controlled by an external (electric or magnetic) field, the application of a strong enough stimulus can result in an elastic deformation of the elastomeric material. Such responsive materials are of particular importance for the design of electromechanical actuators. In general, a rather strong field is required to invoke deformations; however, particular (semi)soft deformation pathways at low free energy cost [1–3] — such as director rotation accompanied by shear — may facilitate the deformation process even in confined (clamped) samples. Experimentally, director response to a normal electric field has been observed in a slab of crosslinked nematic gel, and was seen to be accompanied by shear deformation [4,5]. The corresponding threshold was characterized by a critical electric

field strength rather than by critical voltage as in ordinary liquid crystals. This electromechanical Fréedericksz effect has been explained using the continuum neo-classical rubber elastic theory [5].

The present paper is aimed at studying the same problem, however, by developing and applying a coarse-grained shearable lattice model, an extension of the model presented in Ref. [6]. Our investigation is based on performing extensive Monte Carlo (MC) simulations rather than continuum theory. Apart from the Fréedericksz transition studied in [5], additional structural transitions are observed at field strengths well above the Fréedericksz threshold. Some of the possible structures are shown in Fig. 1. The results are presented in terms of experimental observables: transmitted polarized light intensity patterns and deuterium nuclear magnetic resonance (^{2}H NMR) spectra.

2 Shearable lattice model

In the model, the elastomer is divided into N cells that in the undeformed state when mesogenic units are disordered (isotropic) build up a simple cubic lattice. Assuming that the sample is uniformly crosslinked, lattice points are taken to approximately correspond to crosslinks, while lattice bonds are taken to substitute polymeric chains connecting the neighboring crosslinks. Upon deformation, the displacement of every lattice point is given by the displacement field $\mathbf{v}_i$ $(i = 1..N)$. The average direction of embedded mesogenic units inside each cell is denoted by a unit vector, yielding an orientational field $\mathbf{u}_i$ $(i = 1..N)$. While in Ref. [6] only a homogeneous uniaxial stretch/compress deformation was considered and the director orientation was fixed, such limitations no longer apply to the current modeling. In particular, shear deformations, together with director rotation, are allowed to reproduce (semi)soft elasticity.

The Hamiltonian of the system $\mathcal{H}$ consists of the following contributions: (i) $\mathcal{H}_e$ describing rubber elasticity of polymeric chains, (ii) $\mathcal{H}_n$ describing interactions between mesogenic units and $\mathcal{H}_f$ to model their interaction with the external field, and (iii) $\mathcal{H}_c$, the strain-alignment coupling between polymer chains and mesogenic units.

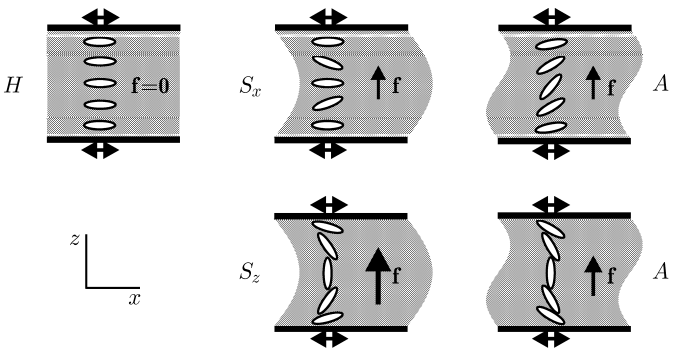

Fig. 1. Schematic depiction of configurations in a planar elastomeric slab exposed to a normal external field **f**, with anchoring along x. In absence of field the homogeneous configuration H is observed. In weak fields the antisymmetric configuration A (two possible versions, depending on the actual field strength) and the symmetric configuration S_x (reported in [1,5]) are seen for weakly and strongly anisotropic networks, respectively. At high field strengths the symmetric S_z structure sets in.

2.1 Polymer chain elasticity

In the description of rubber elasticity we assume that the polymer chains are ideally flexible and do not interact with each other. At this point we also assume that they are not perturbed by the presence of nematogenic units. Then, in the undeformed state, the distribution of chain end-to-end vectors is a three-dimensional Gaussian [1]. Upon deformation, polymer chain trajectories deform affinely together with the sample, which yields a decrease in entropy (increase in free energy). Suppose now that the deformation takes the ith lattice point located initially at $\mathbf{r}_i$ to the new coordinates $\mathbf{r}'_i = \mathbf{r}_i + \mathbf{v}_i$ so that $\mathbf{r}'_i = \lambda_i \mathbf{r}_i$, where $\lambda_i = \partial \mathbf{r}'_i / \partial \mathbf{r}_i$ is the deformation tensor. Its components are

$$\lambda_i^{jk} = \delta^{jk} + \frac{\partial v_i^j}{\partial r_i^k}, \tag{1}$$

where δ^{jk} is the Kronecker symbol, v_i^j stands for the jth component of $\mathbf{v}_i$, and r_i^k represents the kth Cartesian coordinate. For chains with M monomers of length b between crosslinks (at average distance a from each other when the sample is undeformed), the corresponding temperature-dependent pseudo-Hamiltonian can be written as [1,6]

$$\mathcal{H}_e = \frac{3 k_B T a^2}{2 M b^2} \sum_{i=1}^{N} \left[\mathsf{Tr}(\lambda_i {\lambda_i}^T) - 3 \right], \tag{2}$$

where the undeformed sample contribution has been subtracted. In terms of the displacement field $\mathbf{v}_i$ one has

$$\mathsf{Tr}(\lambda_i \lambda_i^T) = 3 + 2 \sum_{k=1}^{3} \frac{\partial v_i^k}{\partial r_i^k} + \sum_{k=1}^{3} \sum_{l=1}^{3} \left(\frac{\partial v_i^k}{\partial r_i^l} \right)^2, \tag{3}$$

and, discretizing derivatives, the elastic pseudo-Hamiltonian, Eq. (2), can be rewritten as

$$\mathcal{H}_e = k_B T \alpha \sum_{[ij]} \left[2 \left(v_j^l - v_i^l \right) + \sum_{k=1}^{3} \left(v_i^k - v_j^k \right)^2 \right], \tag{4}$$

where $\alpha = 3a^2/2Mb^2$. Here $[ij]$ in the outer sum indicates that j is the nearest neighbor of i on the lattice along the increasing lth Cartesian coordinate. (Above, the sum over linear terms has a divergence form: contributions from neighboring unit cells cancel out, except for the contributions at the simulation box surface.) The Hamiltonian $\mathcal{H}_e$ is non-negative upon every deformation and reproduces the effect of entropic elasticity characteristic for rubbers.

2.2 Interactions between mesogenic units and with external field

The interactions between close-packed clusters of embedded mesogenic material (with the average local direction given by $\mathbf{u}_i$) are of dispersive and steric origin. They are modeled via the standard uniaxial Lebwohl-Lasher Hamiltonian [7]

$$\mathcal{H}_n = -\epsilon \sum_{\langle ij \rangle} P_2(\mathbf{u}_i \cdot \mathbf{u}_j), \tag{5}$$

where $P_2(x) \equiv (3x^2 - 1)/2$, $\epsilon > 0$ stands for the strength of the interaction, and the sum goes over nearest neighbor pairs $\langle ij \rangle$. $\mathcal{H}_n$ promotes parallel alignment of mesogenic units, which corresponds to a homogeneous monodomain elastomer that was crosslinked with mesogenic units aligned.

As mesogens are anisotropic dielectrics, they align in an external electric field. In case of elongated molecules with a permanent dipole along the molecular axis the dielectric anisotropy ϵ_a is typically positive and hence molecules are aligned parallel to the field direction. A similar effect is observed in magnetic fields, too. The interac-

tion of mesogenic clusters $\mathbf{u}_i$ with the field is modeled by

$$\mathcal{H}_f = -\epsilon\eta \sum_{i=1}^{N} P_2(\mathbf{u}_i \cdot \mathbf{f}), \tag{6}$$

where the coupling constant η is proportional to the square of the field strength, and $\mathbf{f}$ is a unit vector defining the field orientation. For $\eta > 0$, $\mathbf{u}_i$ align parallel to $\mathbf{f}$. For example, in an electric field η is defined by $\eta = \epsilon_a \epsilon_0 a^3 E^2/3\epsilon$, where E is the field strength and ϵ_0 the dielectric constant of vacuum. Taking $\epsilon_a \sim 6$, $a \sim 4.6$ nm, and $\epsilon \sim 0.023$ eV, $\eta = 0.1$ corresponds to $E \sim 1.44 \times 10^7$ V/m. For simplicity, in the present analysis the external field is assumed homogeneous throughout the sample. This assumption is accurate only if the field is magnetic, or in an electric field for an elastomer with a low enough dielectric anisotropy. In any case this approximation is not expected to be a major one for this work.

2.3 Strain-alignment coupling

Elastomers are known to deform macroscopically upon a change in the orientational ordering (either in the degree of order or in director orientation), which is a consequence of the coupling between mesogenic units and polymer chains [1]. The character of the coupling depends on the detailed architecture of the elastomer; however, materials can be assigned to one of the two main groups, positive and negative materials. In the first group (especially main-chain and some side-chain materials) mesogenic units align along the direction of stretching, while in the second group the alignment is perpendicular. Such behavior can be modeled by a mechanical field acting on the mesogenic units, with a strain-dependent field strength [6]. Alternatively, the strain-alignment coupling can be modeled by coupling the local ordering tensor for mesogenic units

$$\mathsf{Q}_i = \frac{3}{2}(\mathbf{u}_i \otimes \mathbf{u}_i) - \frac{\mathsf{I}}{2} \tag{7}$$

with the local gyration tensor G_i for polymer chains. (Here I represents the unit matrix.) Denoting with $\mathbf{q}_n$ the end-to-end vector for the nth polymer chain in an undeformed sample, close to the ith lattice point after an affine deformation one has $\mathbf{q}'_n = \lambda_i \mathbf{q}_n$. The local gyration tensor is then given by

$$\mathsf{G}_i = \langle \mathbf{q}'_n \otimes \mathbf{q}'_n \rangle_i = \frac{Ma^2}{3} \lambda_i \lambda_i^T, \tag{8}$$

where $\langle \cdots \rangle_i$ stands for averaging over polymer chains [8]. Here it was assumed that the gyration tensor for undeformed polymer chains is isotropic, i. e., $\langle \mathbf{q}_n \otimes \mathbf{q}_n \rangle_i = (Ma^2/3)\mathsf{I}$. Then, any deformation-induced anisotropy of G_i results in an aligning tendency for mesogenic units. Coupling Q_i and G_i, an appropriate scalar invariant becomes $\mathsf{Tr}(\mathsf{Q}_i \mathsf{G}_i) \propto \mathsf{Tr}(\lambda_i \lambda_i^T \mathsf{Q}_i)$ [1,9,10]. This corresponds to a generalization of the mechanical field concept [6] to cases where this field is inhomogeneous and its direction is not fixed. For small deformations one can neglect terms quadratic in $\partial v_i^k / \partial r_i^l$, which also ensures sample stability: the coupling contribution should never overwhelm the positive elastic energy (2). (We will assume that this is qualitatively accurate even outside the small deformation limit. Note that considering linear terms only is compatible with the coupling proposed in Ref. [6] for weak deformations.) Taking, moreover, into account that Q_i is symmetric and

traceless gives

$$\mathsf{Tr}(\lambda_i \lambda_i^T \mathsf{Q}_i) \approx 2 \sum_{k=1}^{3} \sum_{l=1}^{3} Q_i^{kl} \frac{\partial v_i^k}{\partial r_i^l}. \qquad (9)$$

From this one can write for lattice simulation purposes

$$\mathcal{H}_c = -k_B T \chi \sum_{[ij]} \sum_{k=1}^{3} \sum_{l=1}^{3} (Q_i^{kl} + Q_j^{kl})(v_j^k - v_i^k), \qquad (10)$$

where j as in Eq. (4) is the nearest neighbor of i along the increasing lth Cartesian coordinate. Further, χ is the coupling strength parameter: $\chi > 0$ and $\chi < 0$ correspond to positive and negative materials, respectively, and the degree of material anisotropy increases with increasing $|\chi|$. The pseudo-Hamiltonian $\mathcal{H}_c$ scales linearly with temperature, which is due to the assumed entropic origin of the coupling.

3 Monte Carlo simulations and observables

In our Monte Carlo simulations the elastomer slab was sandwiched between two parallel plates lying in xy planes at $z = \pm d/2$. The external field was applied normal to the plates, i. e., along the z axis. The orientations of vectors $\mathbf{u}_i$ in the $z = \pm d/2$ layers were fixed along the x axis to mimic anchoring to solid sample walls, while at the remaining simulation box sides in x and y directions periodic boundary conditions were assumed. Before starting each external field strength scan, a run in absence of the field ($\eta = 0$) was carried out to determine and fix the simulation box dimensions (including d): in case of nematic ordering the system (assumed incompressible) is elongated along the director, x axis, and contracted laterally. Then, to simulate a switching experiment, after equilibration at a given η value, the last sample configuration was used to start a new simulation run at a slightly higher/lower value of η. Typically, 7×10^4 MC cycles were performed both for equilibration and for production. Different sample sizes (from 16^3 to 40^3 unit cells) were considered.

In the MC evolution, the usual Metropolis algorithm [11] was used, and following configurational trial move types were carried out. — Barker-Watts moves [12] reorient mesogenic units $\mathbf{u}_i \to \mathbf{u}_i'$ by randomly choosing both the rotation axis (x, y, or z) and the rotation angle, like in standard Lebwohl-Lasher simulations of liquid crystals [13]. These moves change $\mathcal{H}_n$, $\mathcal{H}_f$, and $\mathcal{H}_c$. — Plane shift moves consist of picking one of the xy lattice planes (perpendicular to the sample normal, z axis) at random and generating a random in-plane shift of the corresponding lattice points. This deforms the initially cubic unit cells into parallelepipeds and thus facilitates the occurrence of shear for (semi)soft elasticity. With this method the geometric compatibility for the λ_i tensor components, as well as the no-displacement boundary condition at the confining plates, are satisfied automatically. Moreover, unit cell volume is conserved, as required by the incompressibility constraint in elastomers. Such moves change $\mathcal{H}_e$ and $\mathcal{H}_c$. — In the case of zero-field pre-scan runs, global rescale moves are performed in addition. In this case the simulation box sides (together with the displacement field $\mathbf{v}_i$) are rescaled at random, but making sure that the volume is kept constant; hence, two out of three box sides are random parameters. These moves are carried out only at $\eta = 0$ before starting the actual η scans, and affect $\mathcal{H}_e$ and

$\mathcal{H}_c$ in the pseudo-Hamiltonian. They deform and displace the confining lower and upper plates, too, keeping the anchoring easy axis (x) fixed. This is equivalent to fitting a spontaneously elongated sample between two confining plates and results in a mechanical field along x. — To ensure efficient MC sampling, trial move amplitudes were adjusted to provide an acceptance ratio close to 50% for each of the trial move types.

To monitor orientational ordering in the system, the order parameter

$$P_2^z = \langle P_2(\mathbf{u}_i \cdot \mathbf{f}) \rangle \tag{11}$$

was calculated, where $\mathbf{f}$ — as above — is a unit vector along the field direction (z axis, sample normal) and $\langle \cdots \rangle$ denotes averaging over volume (i.e., lattice sites) and MC cycles. P_2^z defined in this way is sensitive to both director reorientations and variations in the degree of order, but the latter should be negligible in our case. Hence, below and far above the switching threshold negative (H structure) and positive (S_z structure) values of P_2^z are expected, respectively. Further, to monitor the field-induced deformation, we calculated

$$\mathbf{V} = \langle \mathbf{v}_i - \mathbf{v}_i^\circ \rangle, \tag{12}$$

where $\mathbf{v}_i^\circ$ is the deformation field prior to field application, and $\langle \cdots \rangle$ has the same meaning as above. In the chosen geometry, one expects displacements along the x axis; hence $V_y \approx 0$ and $V_z = 0$ (the latter by definition). Undeformed (H) as well as deformed antisymmetric samples (A) also give $V_x \approx 0$ — recall that $\mathbf{V}$ is defined as volume average —, while $V_x \neq 0$ is a clear signature of symmetrically deformed symmetric samples (S_x and S_z, see Fig. 1). (These remarks will facilitate the interpretation of Fig. 2 later in the manuscript.) — Note that shear deformations with negative and positive x components of the displacement $\mathbf{v}_i - \mathbf{v}_i^\circ$ are degenerate. Both are seen in our simulations.

3.1 Polarized light transmission

As soon as mesogenic units are aligned, the elastomeric material becomes birefringent. In fact, birefringence measurements have been used to explore the optical behavior of LCE under stress [1,14,15]. Here we have used simulated configurations to calculate the intensity patterns of transmitted light when a linearly polarized beam, directed along the y axis, travels through a sample placed between crossed polarizers at $\pm\pi/4$ from the z axis. The phase difference between the ordinary and extraordinary polarization accumulated on passing through a sample

$$\delta = \frac{2\pi d_y \Delta n}{\lambda_0} \tag{13}$$

depends on the the beam path length d_y, light wavelength λ_0, and the refractive index anisotropy Δn. The intensity transmittance for the chosen set-up is given by

$$\mathcal{T} = \sin^2(\delta/2) \cos^2 2\phi \tag{14}$$

and depends on the angle ϕ between the director and the x axis [16]. Consequently, the spatial dependence of ϕ results in characteristic intensity patterns for various director fields shown in Fig. 1.

In the simulation, light propagation through each pixel in the xz-plane was modeled using the Jones matrix approach [16], assuming that local optical axes coincide with

$\mathbf{u}_i$. To increase the optical thickness of the sample, several light passes were allowed for, before calculating the light transmittance $\mathcal{T}(x,z)$ for each pixel. This yields an effective sample thickness equivalent to $d_y \approx 2.2$ μm in the undeformed case, and correspondingly less when the sample is laterally contracted because of ordering along x. The number of light passes was adjusted to give the same d_y for all sample sizes. Other parameters: we assume refractive index anisotropy $\Delta n_0 = 0.2175$ (in case of perfect orientational order) and $\lambda_0 = 632.8$ nm (as for a He-Ne laser in vacuum). Note that in the simulation the optical sample thickness was tuned so as to give $\sin^2(\delta/2)$ rather close to 1; this provides the dark/bright contrast in calculated patterns as high as possible. Diffraction and scattering were neglected [1].

Our system is actually degenerate with respect to x, therefore all quantities depend only on z. For the homogeneous structure H one then has $\phi(z) = 0$, which results in a uniform transmitted pattern with a thickness-dependent intensity. For structure A the dependence $\phi(z)$ is even in z, i. e., $\phi(z) = \phi(-z)$, hence $\mathcal{T}(z) = \mathcal{T}(-z)$: the corresponding transmitted light patterns are symmetric with respect to the central $z = 0$ plane. Note that also for S_x and S_z with odd $\phi(z) = -\phi(-z)$ the transmitted intensity patterns remain symmetric; see Eq. (14). Therefore, the classical set-up between polarizers crossed at $\pi/2$ is inevitably limited in identifying and distinguishing between the simulated structures.

As an alternative, one can use a set-up where the angle between the polarizer and the analyzer is $\pi/4$ rather than $\pi/2$. Then, for the polarizer at $\pi/4$ with respect to the x axis (measured counter-clockwise) and the analyzer along x, the transmittance is given by

$$\mathcal{T}' = \frac{1}{2}\left[1 + \sin^2(\delta/2)\sin 4\phi\right] \tag{15}$$

and is characterized by a different ϕ dependence as above. Now the transmitted light patterns are symmetric with respect to $z = 0$ only for structure A with the even $\phi(z)$ profile, and antisymmetric for structures S_x and S_z with $\phi(z)$ odd. This facilitates the recognition of $A \leftrightarrow S_z$ and $A \leftrightarrow S_x$ transitions that was impossible with the classical set-up.

Note that experimentally switching in elastomers has so far been studied by conoscopy-type experiments where the light is shone along the sample normal (z) [4], which might actually be easier to implement than the set-up proposed here. The current set-up, however, allows for a direct mapping of the $\phi(z)$ director field into a transmittance pattern $\mathcal{T}(z)$, and is in this sense similar to the set-up used in Ref. [17] to visualize the stripe domains when an elastomer is stretched perpendicular to the director.

3.2 Deuterium magnetic resonance

Another powerful method for detecting orientational order in LCE is deuterium magnetic resonance [1,18,19]. Deuterating the mesogenic units (or, alternatively, introducing deuterated mesogenic spin probes into the elastomeric material) results in a orientation-dependent quadrupolar frequency splitting ω_Q that, for the jth mesogenic

cluster, is given by

$$\omega_Q^j = \pm\delta\omega_Q P_2(\mathbf{u}_j \cdot \mathbf{b}), \tag{16}$$

where $\mathbf{b}$ is a unit vector parallel to the NMR spectrometer magnetic field and $\delta\omega_Q$ is a coupling constant [20]. As a result, structures shown in Fig. 1 are expected to give characteristic spectral lineshapes. We have used the simulation output to calculate the spectra by generating the free induction decay signal

$$G(t) = \left\langle \exp\left(i \int_0^t \omega_Q^j(t')\, dt' \right) \right\rangle_j , \tag{17}$$

where $\langle \cdots \rangle_j$ stands for ensemble averaging, and Fourier-transforming it (for details see Ref. [21]). The spectrometer magnetic field was directed along the sample normal, translational diffusion was neglected. The duration of one NMR cycle, $2\pi/\delta\omega_Q$, was fixed to 1024 MC cycles. For smoothening, a convolution with a Lorentzian kernel of width $0.02\delta\omega_Q$ was applied.

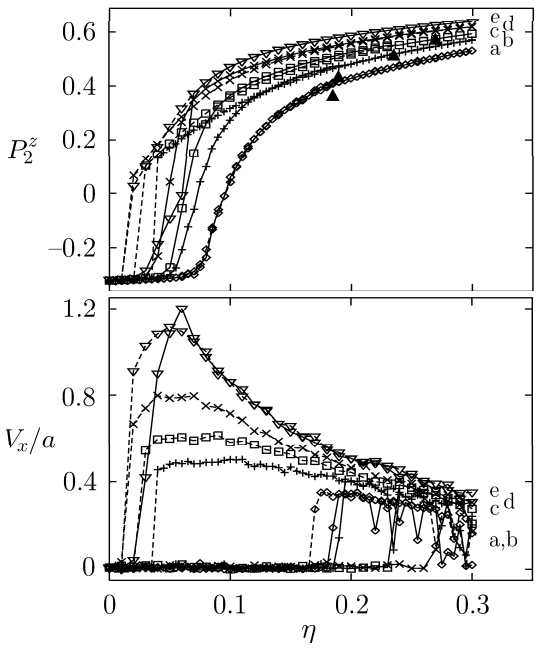

Fig. 2. External field strength scans in a weakly anisotropic elastomeric slab ($\chi = 0.1$) at $T^* = 1.0$. $P_2^z(\eta)$ (*top*) and $V_x(\eta)$ (*bottom*) dependences are plotted for different sample sizes: 16^3 (a), 20^3 (b), 24^3 (c), 30^3 (d), and 40^3 (e). Solid and dashed lines correspond to increasing and decreasing η, respectively; note the hysteresis. The $H \to S_x$ transition is seen only for $N = 40^3$ (triangles), otherwise $H \to A$ is observed. In the upper plot, arrows indicate the approximate position of the $A \to S_z$ transition (for $N \leq 30^3$) clearly visible in the lower plot.

The above calculation of NMR spectra is based on the orientational dynamics of mesogens generated by the Metropolis algorithm (rather than by equations of motion). It consists of Barker-Watts reorienting moves that are similar to natural mesogen dynamics, and of collective plane shift moves. Once the system is equilibrated, the amplitude of the shift moves becomes small and the major contribution to the dynamics comes from mesogen reorientations. We therefore believe that the Metropolis algorithm still provides a realistic enough sequence of Monte Carlo configurations to be used for the calculation of NMR spectra [21].

4 Results

All simulations were run at $T^* = k_B T/\epsilon = 1.0$ well inside the aligned nematic phase [6]. Consider first a weakly anisotropic positive elastomeric material with $\chi = 0.1$ in the absence of an external field. This choice for χ is equivalent to the coupling constant value used in Ref. [6]. As the director was fixed by anchoring, there is a sponta-

neous sample elongation along x, the easy axis. This elongation establishes a mechanical field parallel to x and is accompanied by lateral contraction, as required by the incompressibility constraint. The equilibrium box shape depends somewhat on the sample dimension; on average, however, our initially cubic unit cells deform into boxes with approximate dimensions $1.12a \times 0.96a \times 0.93a$. There is weak systematic biaxiality in the lateral contraction that stems from the inequivalence of the y and z directions due to the presence of confinement. For $\eta = 0$ the system is on average homogeneous and thus corresponds to the H-structure.

Starting the external field scan with $\eta > 0$, the mismatch between the mechanical and the external field (directed along x and z, respectively) below the switching threshold results merely in a slight decrease in the degree of ordering, while the director remains homogeneous. Then, at the threshold, the director reorients, which is accompanied by a spontaneous elastic shear deformation; see Figs. 2-4. In small samples ($N \leq 30^3$) the resulting configuration is the antisymmetric structure A: the wavelength of the director field distortion is equal to $2d_z$ — twice the distance between the confining plates — like for the standard Fréedericksz transition in nematics, while for the accompanying elastic shear deformation it equals d_z. Considering the sign of the λ_i^{xz} deformation tensor component, along the z axis three domains appear. Two different A configurations can be observed, depending on the η value: the upper A in Fig. 1 is seen for smaller η than the lower one. In the former case, the director in the center of the sample is directed along the local extension, as favored by the strain-alignment coupling $\mathcal{H}_c$ (10), while in the latter it is parallel to the external field.

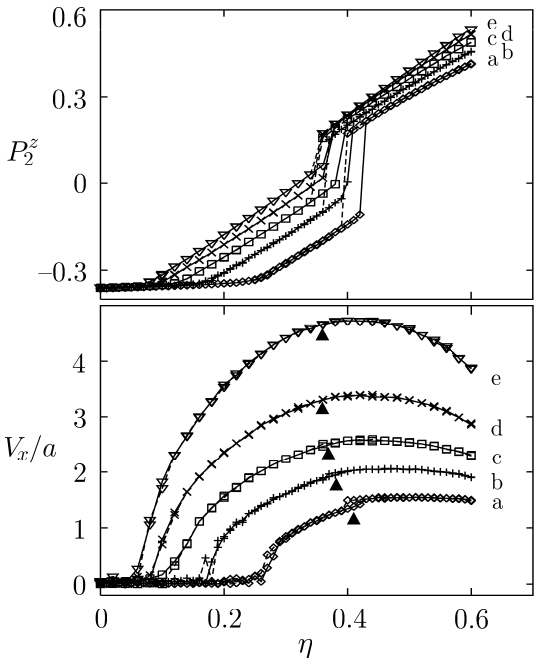

Fig. 6. Same as Fig. 2, but for a strongly anisotropic elastomer ($\chi = 0.3$). Here the arrows indicate the approximate position of the $S_x \leftrightarrow S_z$ transition.

The transition $H \rightarrow A$ is characterized by a sudden increase of the P_2^z order parameter, while the average displacement V_x, being a bulk average, remains close to 0 (Fig. 2). When the sample is put between polarizers crossed at $\pi/2$ and η is increased, the transmitted light intensity (Fig. 3a,b) starts from bright throughout the sample (corresponding to $\phi \sim 0$, H structure), changes to dark in the central layers ($\phi \sim \pi/4$) above the threshold, and goes back to bright in the field-aligned central region ($\phi \sim \pi/2$), with some dark stripes originating from the residual substrate-induced tilt. As predicted, all patterns are symmetric. The alternative optical set-up with the po-

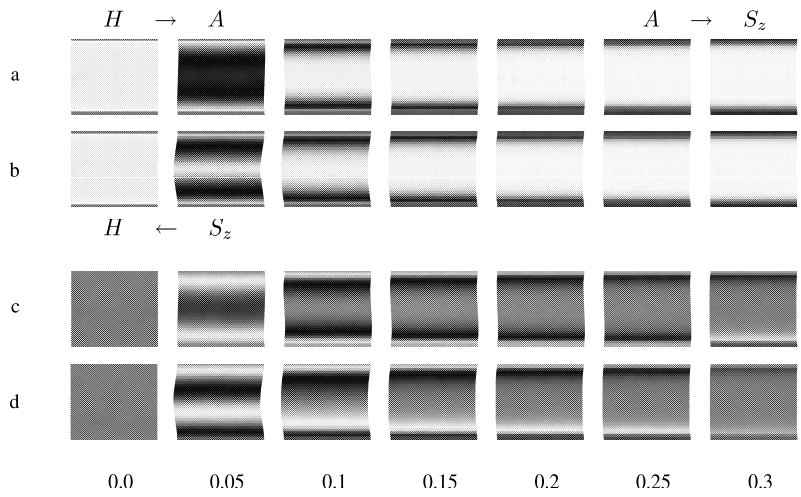

Fig. 3. Patterns of transmitted light intensity in a weakly anisotropic elastomer ($\chi = 0.1$), with visualized shear deformation; $N = 30^3$. Classical (a,b) and alternative (c,d) polarizer set-up. Scans with increasing (a,c) and decreasing (b,d) field strength, with the corresponding η values reported below. Hysteresis $H \to A \to S_z \to H$ is visible.

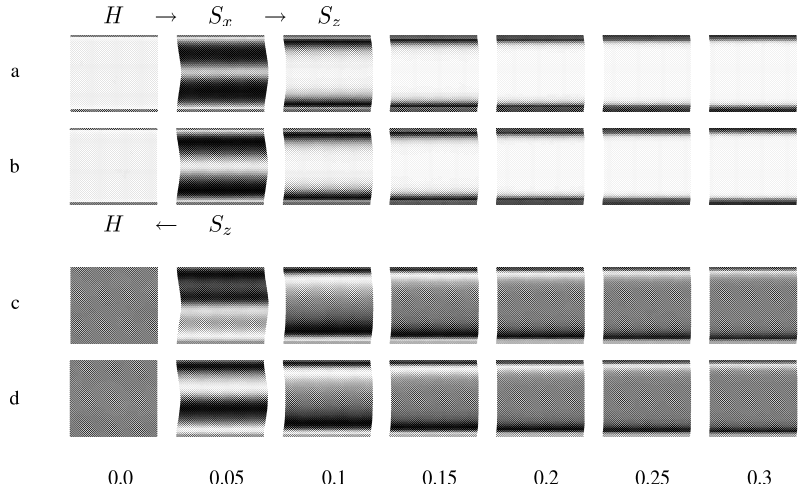

Fig. 4. Same as Fig. 3, but for $N = 40^3$. Hysteresis $H \to S_x \to S_z \to H$ is visible.

larizer and analyzer at $\pi/4$ (Fig. 3c,d) also yields symmetric intensity patterns, with maxima at $\phi = \pi/8, -3\pi/8$ and minima at $\phi = -\pi/8, 3\pi/8$. The anchoring-aligned H structure with $\phi = 0$, as well as the field-aligned structures with $\phi \sim \pi/2$ in central layers, yield a 50% transmittance resulting in a gray display. — The corresponding ^{2}H NMR spectra, Fig. 5, provide a similar picture of the $H \to A$ switching: below the threshold the sample is aligned along the x axis (i. e., perpendicular to **b**, the spectrometer magnetic field), with two well-resolved spec-

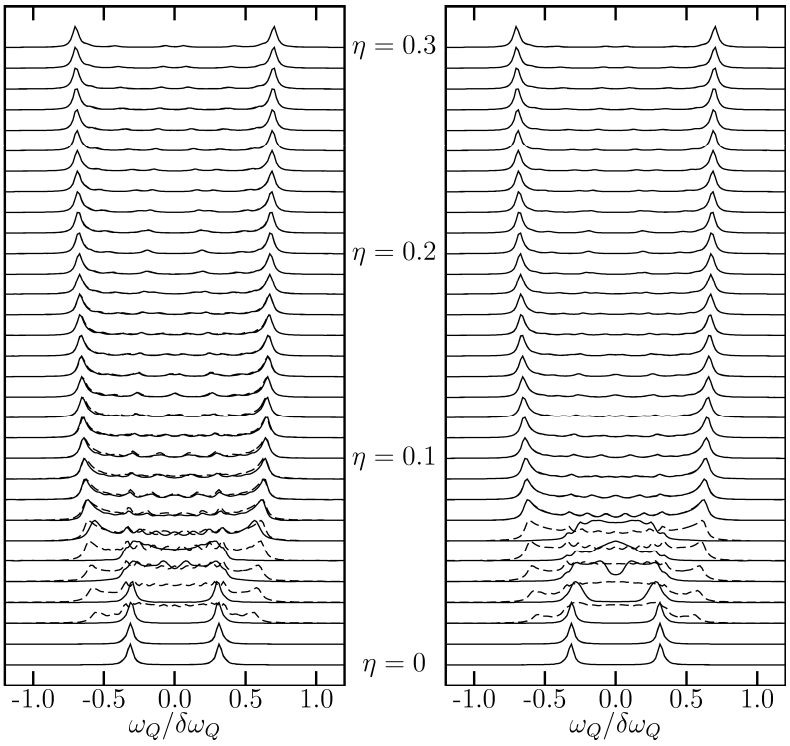

Fig. 5. ^{2}H NMR spectra in a weakly anisotropic elastomer ($\chi = 0.1$), $N = 30^3$ (*left*) and $N = 40^3$ (*right*). It is difficult to distinguish the spectra for the $N = 30^3$ sample following the $H \to A \to S_z$ pathway on increasing η, and the larger $N = 40^3$ one characterized by a different $H \to S_x \to S_z$ sequence. The hysteresis is visible (solid and dashed lines correspond to increasing and decreasing η, respectively).

tral peaks at a splitting $\mp\delta\omega_Q P_2^z/2$, and above it massive field-induced alignment in the z direction (coinciding with **b**) is observed, eventually yielding a two-peak spectrum with a splitting equal to $\pm\delta\omega_Q P_2^z$. Residual surface-induced alignment along the x axis is visible even above the threshold.

In large samples ($N \geq 40^3$), however, we observe a transition to the symmetric S_x (rather than to antisymmetric A) structure predicted in Ref. [5], where the alignment along x in the central $z = 0$ layer is stabilized by the mechanical field. Moreover, in larger samples Hamiltonian gradient terms related to spatial director variation (5) play a less important role. The wavelengths of the director and elastic distortion are now d_z and $2d_z$, respectively, just the opposite as in small samples. Note that here only two (rather than three) shear domains are created, which leads to a nonzero effective deformation in the x direction: $V_x \neq 0$ (Fig. 2). — Above the threshold, the classical optical set-up (Fig. 4a,b) gives a symmetric transmitted pattern for the S_x structure, with a bright stripe in central layers already at the threshold (contrary to the A structure), corresponding to the persisting $\phi \sim 0$ alignment in this region. The alternative optical set-up (Fig. 4c,d), however, gives antisymmetric patterns quite different from the

ones seen for the A structure. — The calculated ^{2}H NMR spectra, Fig. 5, are too similar to the ones obtained in small samples to allow for a clear distinction between the A and S_x structures. Indeed, the quadrupolar splitting ω_Q is for $\mathbf{b}||\mathbf{f}$ proportional to $P_2(\cos\phi)$, so the director orientations $\pm\phi$ cannot be distinguished. However, a distinction between A and S_x would be facilitated if the sample was rotated about an axis perpendicular to $\mathbf{b}$ in order to lift the degeneracy of the $\pm\phi$ orientations, and the full angular dependence of the spectra was recorded. These measurements seem possible and we hope they will be performed since they would provide an important test of our and other theoretical methods.

As one can deduce from Fig. 2, for the transitions $H \rightarrow A$ and $H \rightarrow S_x$ the corresponding η thresholds decrease with increasing sample size (see Table 1). The dependence is less pronounced in large samples where the gradient terms related to surface boundary conditions become less important. In very large samples the threshold seems to approach 0, which is in agreement with the fact that the coupling term in the Hamiltonian, $\mathsf{Tr}(\lambda_i\lambda_i^T\mathsf{Q}_i)$, allows ideally soft deformations [1]. (Note that our modeling applies to the static case and that controversies regarding dynamic soft elasticity [22] cannot be answered here.) On the other hand, experiments have shown that the $H \rightarrow S_x$ switching in elastomers is actually characterized by a nonzero threshold even in large samples [4, 5], but in that case the existence of a switching threshold could be attributed to the intrinsic semisoftness of the elastomer (not included in our modeling). Note also that experimentally in small samples $H \rightarrow A$ transitions are observed, too [5].

In rather strong external fields, both in small and large samples (i. e., from A and S_x structures) a second transition is observed, resulting in the symmetric S_z structure. Here the wavelengths for director and elastic distortion both equal $2d_z$, and the director is aligned along z even in the central layer of the sample. The $A \rightarrow S_z$ transition reflects in a jump of V_x to a nonzero value; $S_x \rightarrow S_z$, however, in a jump of P_2^z becoming less and less pronounced with increasing sample size (Fig. 2). As for progressive alignment along z the occurrence of shear becomes less favorable, the effective deformation V_x decreases with increasing η. Hence, V_x peaks at a certain value of η which may be important for the optimization of the actuation process. For the $A \rightarrow S_z$ transition (in small samples) the threshold increases with sample size, while for the $S_x \rightarrow S_z$ transition (in large enough samples) it seems to be fairly sample size-independent as it involves only a thin wall between domains of opposite shear. In large enough samples the thickness of the domain wall (a few lattice spacings) becomes sample size-independent, too. — Analyzing the optical transmission data, Figs. 3-4, the alternative set-up turns out to be suitable for the detection of the $S_x \rightarrow S_z$ transition, and, moreover, always offers a reliable detection of the $A \rightarrow S_z$ transition since it is characterized by a very evident change in symmetry of the transmission pattern. — Eventually, ^{2}H NMR, Fig. 5, seems to be unable to detect the $A \rightarrow S_z$ and $S_x \rightarrow S_z$ transitions: the fraction of the reoriented elastomeric ma-

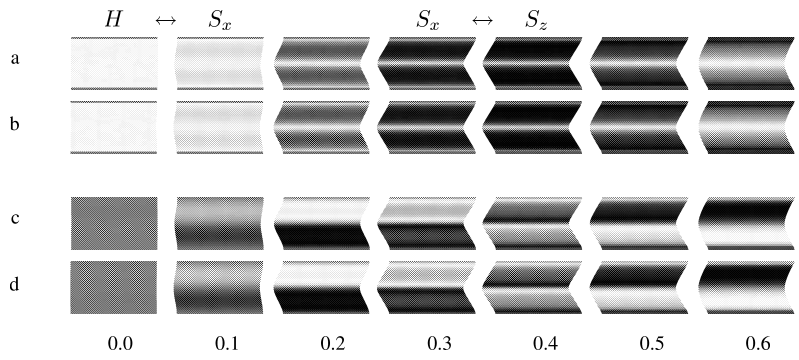

Fig. 7. Same as Fig. 3, however, for a strongly anisotropic sample with $\chi = 0.3$ and $N = 30^3$. No hysteresis can be observed.

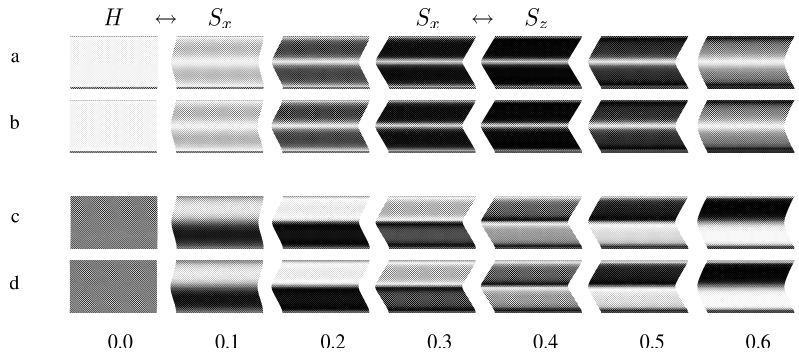

Fig. 8. Same as Fig. 7, but for $N = 40^3$. No hysteresis is visible.

terial is too small to be detectable within the bulk response of the system. — On decreasing η, for all sample sizes except for $N = 16^3$ a large hysteresis and a direct transition $S_z \rightarrow H$ are observed, which can be deduced from the simulated observables. The small $N = 16^3$ sample, however, follows the $S_z \rightarrow A \rightarrow H$ route like on increasing η, with a weak hysteresis only at the $A \rightarrow H$ transition.

Turn now to samples with a stronger strain-alignment coupling, i. e., to $\chi = 0.3$. The zero-field equilibration run results in a simulation box that is more anisotropic than for $\chi = 0.1$, with average unit cell dimensions $1.44a \times 0.85a \times 0.82a$. This results in a stronger mechanical field along x, and in the external field scan even for the smallest sample considered the switching from the undeformed H structure always gives the S_x structure, which differs from the behavior observed in ordinary nematics and in small elastomeric samples. (Here the alignment along x at $z = 0$ seems to be stabilized by the strong mechanical field.) The $H \rightarrow S_x$ transition is easily detected from the $P_2^z(\eta)$ and $V_x(\eta)$ dependences shown in Fig. 6, and occurs at a higher field strength if compared with the $\chi = 0.1$ case. Moreover, both dependences are less abrupt than for $\chi = 0.1$. Here too the threshold is sample size-dependent, but, as before, the dependence becomes weaker

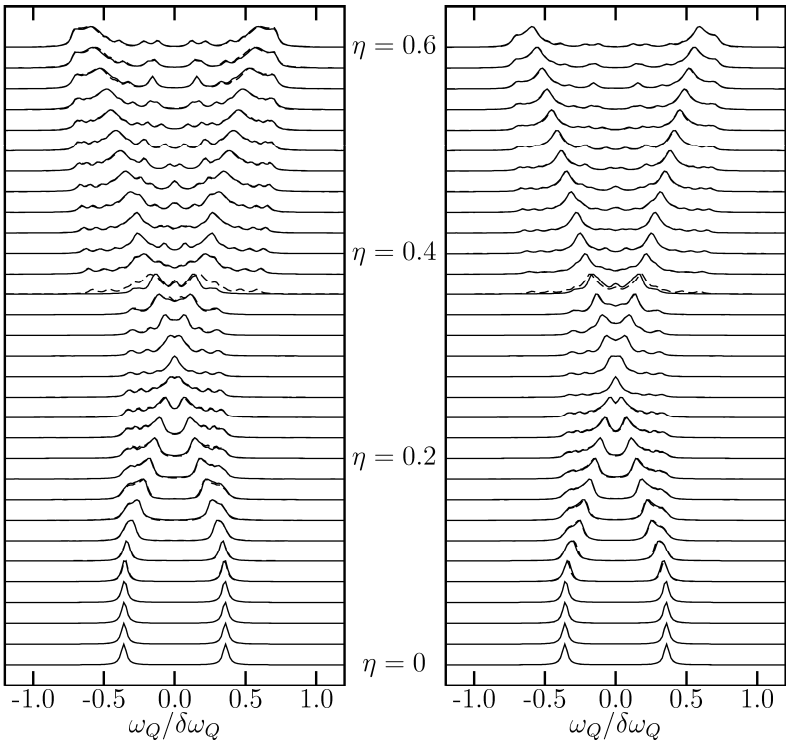

Fig. 9. Same as Fig. 5, but for higher anisotropy of the elastomer ($\chi = 0.3$). The spectral sets for $N = 30^3$ (*left*) and $N = 40^3$ (*right*) are again very similar. The hysteresis is less pronounced.

Table 1. Summary of approximate η thresholds for various structural transitions. For $\chi = 0.1$ and $\chi = 0.3$ the absolute errors are estimated as ± 0.005 and ± 0.01, respectively.

N	χ	$H \to A$	$A \to S_z$	$S_z \to A$	$A \to H$	$H \to S_x$	$S_x \to S_z$	$S_z \to H$	$S_z \to S_x$	$S_x \to H$
16^3	0.1	0.075	0.185	0.17	0.075	—	—	—	—	—
20^3	0.1	0.055	0.19	—	—	—	—	0.04	—	—
24^3	0.1	0.045	0.235	—	—	—	—	0.03	—	—
30^3	0.1	0.035	0.27	—	—	—	—	0.02	—	—
40^3	0.1	—	—	—	—	0.025	0.065	0.02	—	—
16^3	0.3	—	—	—	—	0.26	0.425	—	0.395	0.26
20^3	0.3	—	—	—	—	0.17	0.40	—	0.365	0.17
24^3	0.3	—	—	—	—	0.11	0.39	—	0.35	0.11
30^3	0.3	—	—	—	—	0.08	0.37	—	0.35	0.08
40^3	0.3	—	—	—	—	0.06	0.37	—	0.35	0.06

with increasing sample size. Within the current scan resolution, there is no observable hysteresis for the $H \leftrightarrow S_x$ switching. Like for $\chi = 0.1$, in a strong enough external field there is a second transition to the S_z structure. The transition $S_x \leftrightarrow S_z$ shows only a weak hysteresis and is almost sample size-independent since it involves only a thin domain wall in the central layer of the simulation box. — The calculated optical patterns (Figs. 7-8), as well as ^{2}H NMR spectra (Fig. 9), all reveal the more gradual character of the switching in comparison with the less anisotropic $\chi = 0.1$ elastomeric material. — Finally note that the calculated spectra mainly consist of doublets and that apparently there is no sizable distribution of ϕ in our samples: the mesogenic units seem to be well aligned either along the external or the strain-induced mechanical field. The only exceptions are the thin subsurface regions where anchoring effects become important, as well as the also thin shear domain wall(s).

5 Conclusions

We have developed a shearable coarse-grained lattice model for liquid-crystalline elastomers. In these systems, the possibility of describing shear is essential for the occurrence of (semi)soft elasticity. The model was used to study external field-induced structural transitions in an elastomeric slab and the numeric output was used to predict transmitted light intensity patterns for a sample between polarizers, as well as ^{2}H NMR spectra. The switching features in small samples are similar to those observed in ordinary nematics, with increasing sample size (or, alternatively, the anisotropy of the elastomeric material), however, a qualitatively different behavior is observed. In more anisotropic elastomers the switching thresholds are higher and the switching becomes more gradual.

This work was carried out within the FULCE (Functional Liquid Crystalline Elastomers) Research Training Network funded by the European Union. Further financial support of MIUR COFIN (Cristalli Liquidi) and of MVZT (project J1-6539-0106-04) is acknowledged.

References

1. M. Warner and E. M. Terentjev, *Liquid Crystal Elastomers* (Oxford University Press, Oxford 2003).
2. L. Golubović and T. C. Lubensky, Phys. Rev. Lett. **63**, (1989) 1082.
3. P. D. Olmsted, J. Phys. II France **4**, (1994) 2215.
4. C.-C. Chang, L.-C. Chien, and R. B. Meyer, Phys. Rev. E **56**, (1997) 595.
5. E. M. Terentjev, M. Warner, R. B. Meyer, and J. Yamamoto, Phys. Rev. E **60**, (1999) 1872.
6. P. Pasini, G. Skačej, and C. Zannoni, Chem. Phys. Lett. **413**, (2005) 463.
7. P. A. Lebwohl and G. Lasher, Phys. Rev. A **6**, (1972) 426.
8. P. D. Olmsted and S. M. Milner, Macromolecules **27**, (1994) 6648.
9. P. G. de Gennes, C. R. Acad. Sc. Paris **281**, (1975) 101.
10. N. Uchida and A. Onuki, Europhys. Lett. **45**, (1999) 341.
11. N. Metropolis, A. W. Rosenbluth, M. N. Rosenbluth, A. H. Teller, and E. Teller, J. Chem. Phys. **21**, (1953) 1087.
12. J. A. Barker and R. O. Watts, Chem. Phys. Lett. **3**, (1969) 144.

13. U. Fabbri and C. Zannoni, Mol. Phys. **58**, (1986) 763.

14. J. Küpfer and H. Finkelmann, Macromol. Chem. Rapid Commun. **12**, (1991) 717.

15. W. Kaufhold, H. Finkelmann, and H. R. Brand, Makromol. Chem. **192**, (1991) 2555.

16. P. J. Collings and J. S. Patel, *Handbook of Liquid Crystal Research* (Oxford University Press, New York 1997).

17. I. Kundler and H. Finkelmann, Macromol. Chem. Rapid Commun. **16**, (1995) 697.

18. S. Disch, C. Schmidt, and H. Finkelmann, Macromol. Rapid Commun. **15**, (1994) 303.

19. A. Lebar, Z. Kutnjak, S. Žumer, H. Finkelmann, A. Sánchez-Ferrer, and B. Zalar, Phys. Rev. Lett. **94**, (2005) 197801.

20. A. Abragam, *The Principles of Nuclear Magnetism* (Clarendon Press, Oxford 1961).

21. C. Chiccoli, P. Pasini, G. Skačej, S. Žumer, and C. Zannoni, Phys. Rev. E **60**, (1999) 4219.

22. P. Martinoty, P. Stein, H. Finkelmann, H. Pleiner, and H. R. Brand, Eur. Phys. J. E **14**, (2004) 311.